Nonlinear effects of variable bathymetry and free surface on mini-tsunamis generated by a moving ship

Jinyu Yao [1], Harry B. Bingham [2], and Xinshu Zhang [1,*]

[1] *State Key Laboratory of Ocean Engineering, Shanghai Jiao Tong University, Shanghai 200240, China*

[2] *Department of Civil & Mechanical Engineering, Technical University of Denmark, Lyngby, Denmark*

(Received 7 July 2023; accepted 30 August 2023; published 14 September 2023)

The mini-tsunami phenomenon denotes a newly observed upstream wave generated by a ship traveling across a depth change at subcritical speed. In this study, a high-order spectral model with variable bathymetry (HOS-VB) is developed to study the effects of bottom and free-surface nonlinearities on the generation and propagation of mini-tsunamis over a range of depth-based Froude number Fr_0, average water depth to ship draft ratio h_0/d, bathymetric slope variation γ, and channel width to ship width ratio W/B. The analyses show that the wave amplitude of the mini-tsunamis is increased by both bottom and free-surface nonlinearities and that the influence of free-surface nonlinearities on the wave amplitude is more significant in a narrower channel. Second-order free-surface nonlinearities provide the most important contribution. Compared with linear results, second-order free-surface nonlinearities can more than double the maximum wave amplitude and induce a substantial increase in the mean free-surface level for a narrow channel at large Froude number. The wavelength at half-crest height is also increased by second-order free-surface nonlinearities, and this effect is enhanced as h_0/d decreases. Moreover, the increasing trend of wave amplitude with Fr_0 and the decreasing trend of wave amplitude with h_0/d are more significant as the free-surface nonlinearity increases.

DOI: 10.1103/PhysRevFluids.8.094801

I. INTRODUCTION

A new type of upstream wave, whose generation mechanism is distinctive from that of nonlinear solitons, was observed in a harbor at Flaskebekk, Oslofjorden, Norway [1]. It is generated when a large ship sails through a water with a change in depth at a subcritical speed. The difference between the water depths in the deep and shallow regions, denoted by Δh, is comparable to the average depth h_0, $\Delta h/h_0 \sim 1$. The Froude number $\mathrm{Fr}_0 = U_0/\sqrt{gh_0}$, based on the average water depth h_0, ranges from 0.4 to 0.7, where U_0 is the ship speed and g is the gravitational acceleration. Although the amplitudes of the upstream waves are smaller than those of tsunamis, the generation mechanisms are similar. Therefore, this new type of ship-induced wave is denoted as a "mini-tsunami." Mini-tsunamis observed at Flaskebekk are 0.5–1 km long, with a maximum wave height of approximately 1.4 m. The period ranges between 30 and 60 s, and the waves extend across a 2–3-km-wide fjord. According to testimonies collected from the residents of the Flaskebekk village, mini-tsunamis can cause significant coastline erosion.

Most of the previous studies on ship-induced waves considered a ship moving over a flat topography. Ship-induced waves consist of wake waves and upstream waves, whereas the latter only exist under certain conditions. These waves not only erode the seafloor and coastlines, but also

*xinshuz@sjtu.edu.cn

pose a threat to human safety, such as the fatal accidents that occurred in Harwich, a port in England [2].

The waves generated by a ship in steady motion vary with Froude number $\mathrm{Fr} = U_0/\sqrt{gh}$ with h being the water depth. When a ship travels at a subcritical speed ($\mathrm{Fr} < 1$) over a flat bottom, a wave wake and a depression are formed along the ship. The depressions can travel long distances and become asymmetric during their propagation [3]. Meanwhile, a downward force and a trimming moment act on the ship, causing a phenomenon named "squat," which becomes more substantial as Fr increases [4]. Tuck [5] proposed a slender-body theory by matched asymptotic expansions to evaluate the hydrodynamic force acting on a sailing ship in an unbounded waterway. Subsequently, this method was extended to study the squatting of a ship moving in a dredged channel and in a canal with a restricted width [6,7].

In near-critical ($\mathrm{Fr} \sim 1$) and supercritical ($\mathrm{Fr} > 1$) conditions, nonlinear effects become dominant. The Korteweg–de Vries (Kdv) and Boussinesq equations have been used to study the generation mechanism and the stability of upstream solitons [8–11]. Solitons which are continuously generated at the bow have a mean free-surface level above the still free surface and propagate forward at a supercritical speed. In a channel with restricted width, the crestlines of the solitons are straight lines, and the solitons begin to break at $\mathrm{Fr} = 1.2$ becoming a hydraulic jump at $\mathrm{Fr} = 1.3$ [12]. However, in an unbounded shallow-water region, the crestline is parabolic and the solitons do not break at $\mathrm{Fr} = 1.2$, but form several parabolic water humps that are blocked ahead of the ship [13]. In a uniform current, the maximum water level elevation of ship-induced waves is more significant than that of ship-induced waves without a current [14].

The above mentioned studies focused on cases with flat topography, while ship-induced waves propagating in a channel with a variable cross-channel depth have also been investigated in several studies. Boussinesq equations have been extended to address the bottom variations [15–17]. Wei *et al.* [18] improved the linear dispersion properties in intermediate water depths by using the velocity at a certain depth as the expansion variable to derive fully nonlinear extended Boussinesq equations which are implemented in the FUNWAVE code. Torsvik *et al.* [19] adopted the COULWAVE model, which has an algorithm similar to that proposed by Wei *et al.* [18], to investigate the impact of cross-channel depth variation on ship wave patterns. Both the upstream waves and wake waves are amplified as they propagate towards the shore. The crestlines of the upstream waves remain straight despite the variation in depth across the channel. Breaking of diverging waves from the ship occurs as they propagate towards the shore. The crestline of the diverging waves is bent towards the shore, and the wave refraction over the slope does not follow Snell's law [20]. In addition, the ship-induced waves can contribute to wave wash and become the driving force for shoreline erosion [21,22].

The interaction between a traveling ship and a change in water depth along the ship track results in the generation of mini-tsunamis [1]. Motivated by the erosion effect of mini-tsunamis, Grue [1] ingeniously proposed a linear model in which an advancing ship is modeled by a moving pressure distribution to investigate the influence of the Froude number and channel width on the height and wavelength of the mini-tsunamis. Mini-tsunamis are followed by several short waves, and the generation of these is attributed to the gradients of the ship pressure [23].

It is noted that linear free-surface boundary conditions were used in the aforementioned studies conducted by Grue [1,23]. Nonlinear effects could play an important role in rogue waves generated by depth variations [24,25]; however, nonlinear effects on mini-tsunamis remain unclear. Because larger waves cause more severe coastal erosion, taking nonlinear effects into account might help prevent underestimation of coastal erosion effects due to underestimation of wave energy. This is the motivation for the present study, where we mainly focus on the generation mechanism and nonlinear evolution of mini-tsunamis and investigate the nonlinear effects on the characteristics of mini-tsunamis, namely, the wave amplitude A, the wavelength at half-crest height $\lambda_{1/2}$, and the phase velocity c. A high-order spectral model with variable bathymetry, called HOS-VB, is developed to simulate the evolution of mini-tsunamis over a variable bathymetry under different conditions where the Froude number based on the average depth Fr_0, the ratio of average depth

to the ship draft h_0/d, the slope of the depth variation γ, and the ratio of the channel width to the ship width W/B are the main parameters. The results of the HOS-VB and the fully nonlinear Boussinesq model, FUNWAVE-TVD, are compared to determine the reliability of the HOS-VB computations. By comparing results from HOS-VB and the linear model proposed by Grue [1], we examine the influence of bottom and free-surface nonlinearities on mini-tsunamis. Both wave amplitude and wavelength are increased by higher-order nonlinearities. Second-order free-surface nonlinearities provide the most important contribution; they can more than double the amplitude of the mini-tsunamis when a ship travels with a large Fr_0 in a narrow channel. Nonlinear effects are more significant in conditions with larger Fr_0 and smaller h_0/d or W/B.

The remainder of this paper is organized as follows. The numerical models are introduced in Sec. II. The setup of the numerical simulation and a detailed description of the test cases are presented in Sec. III. In Sec. IV the numerical model, HOS-VB, is validated by comparing the numerical results with the experimentally obtained gauge records and the data measured by a wave radar, respectively. The generation and propagation of mini-tsunamis are discussed in Sec. V. In Sec. VI the nonlinear effects resulting from the variable topography and free surface on the characteristics of mini-tsunamis are discussed. Finally, conclusions are presented in Sec. VII.

II. HIGH-ORDER SPECTRAL MODEL WITH VARIABLE BATHYMETRY

The high-order spectral model with variable bathymetry (HOS-VB) is based on the potential flow formalism and directly solves the field equation with the kinematic and dynamic boundary conditions on the free surface in the Zakharov form. The flow can be described by a velocity potential $\phi(x, y, z)$, where x and y are the two horizontal axes, and z is the vertical axis pointing upwards. The mean water surface level is at $z = 0$. The velocity potential ϕ satisfies the Laplace equation:

$$\Delta\phi = 0. \tag{1}$$

The free-surface velocity potential $\phi^S(x, y, t) = \phi(x, y, \eta(x, y, t), t)$ is introduced here, such that the nonlinear free-surface boundary conditions are

$$\eta_t = (1 + \nabla\eta \cdot \nabla\eta)\phi_z - \nabla\phi^S \cdot \nabla\eta, \quad \text{on } z = \eta(x, y, t), \tag{2}$$

$$\phi^S_t = -g\eta + \tfrac{1}{2}(1 + \nabla\eta \cdot \nabla\eta)\phi_z^2 - \tfrac{1}{2}\nabla\phi^S \cdot \nabla\phi^S - \frac{p}{\rho}, \quad \text{on } z = \eta(x, y, t), \tag{3}$$

where $\nabla = (\frac{\partial}{\partial x}, \frac{\partial}{\partial y})$, η is the free-surface elevation, and ρ and g are the water density and gravitational acceleration, respectively. Detailed information about the moving pressure p is introduced in Sec. III A. Periodic boundary conditions are used in the horizontal plane.

The total water depth h can be decomposed into the average depth h_0 and the bottom variation β: $-h = -h_0 + \beta(x, y)$. The bottom boundary condition is as follows:

$$\nabla\phi \cdot \nabla\beta - \phi_z = 0, \quad \text{on } z = -h_0 + \beta(x, y). \tag{4}$$

After the vertical velocity on the free surface, denoted by $\phi_z(x, y, z = \eta)$, is obtained, ϕ and η can be time stepped based on Eqs. (2) and (3). A fourth-order Runge-Kutta method is used for the time stepping. The sawtooth instabilities due to the aliasing in the HOS-VB are controlled using a low-pass filter. The values of the parameters in the filter are critical to the reliability of the results; the details are provided in Appendix A.

The velocity potential is expressed as a truncated power series of components $\phi^{(m)}$ for $m = 1$ to M (see [26,27]),

$$\phi = \sum_{m=1}^{M} \phi^{(m)}. \tag{5}$$

To account for the variable depth, the potentials at different orders are written as

$$\phi^{(m)} = \phi_{h_0}^{(m)} + \phi_{\beta}^{(m)}, \tag{6}$$

where the total velocity potential $\phi^{(m)}$ is decomposed into two terms: one is the potential derived at the average depth, $\phi_{h_0}^{(m)}$, while the other is induced by the bottom variation, $\phi_{\beta}^{(m)}$. Correspondingly, $\phi_{h_0}^{(m)}$ should satisfy the boundary condition on the mean bottom level:

$$\frac{\partial \phi_{h_0}^{(m)}}{\partial z} = 0, \quad \text{on } z = -h_0. \tag{7}$$

$\phi_{\beta}^{(m)}$ allows us to define the condition of Eq. (4) for the variable bottom and satisfies a Dirichlet condition on the still water surface:

$$\phi_{\beta}^{(m)} = 0, \quad \text{on } z = 0. \tag{8}$$

Therefore, $\phi_{h_0}^{(m)}$ and $\phi_{\beta}^{(m)}$ are expressed as follows:

$$\phi_{h_0}^{(m)} = \sum_p \sum_q A_{pq}^{(m)}(t) \frac{\cosh[k_{pq}(z+h_0)]}{\cosh(k_{pq}h_0)} e^{i(k_{xp}x + k_{yq}y)}, \tag{9}$$

$$\phi_{\beta}^{(m)} = \sum_p \sum_q B_{pq}^{(m)}(t) \frac{\sinh(k_{pq}z)}{\cosh(k_{pq}h_0)} e^{i(k_{xp}x + k_{yq}y)}, \tag{10}$$

where $k_{xp} = 2\pi p/L_x$, $k_{yq} = 2\pi q/L_y$, and $k_{pq} = \sqrt{k_{xp}^2 + k_{yq}^2}$. L_x and L_y are the lengths of computational domain in the x and y directions, respectively. The Fast Fourier Transform method is used to compute the modal amplitudes $A_{pq}^{(m)}(t)$ and $B_{pq}^{(m)}(t)$. More specifically, $A_{pq}^{(m)}(t)$ can be computed based on Eqs. (2), (3), and (7), then $B_{pq}^{(m)}(t)$ is computed as follows.

Following Eq. (5), the total potential ϕ is truncated at order M; therefore, by substituting Eq. (5) into Eq. (4), the bottom boundary condition can be also truncated at order M (M is the order of free-surface nonlinearity). At each order of m, based on the assumption that $\frac{\beta}{h_0} \ll 1$, $O(\frac{\beta}{h_0}) \equiv O(\frac{\partial \beta}{\partial x}) \equiv O(\frac{\partial \beta}{\partial y})$, the bottom boundary condition can be expanded with respect to the average depth $z = -h_0$, and truncated to order M_b (M_b is the order of bottom nonlinearity). If $M_b = 0$, a flat topography corresponding to the average water depth is used. If $M_b \geqslant 1$, bathymetric variation is considered, and the corresponding water depth is expressed by $-h_0 + \beta(x, y)$. The increase of M_b does not affect the variable bathymetry but decreases the truncation error of the velocity potential. According to Eq. (6), the total potential $\phi^{(m)}$ is decomposed into two parts, $\phi_{h_0}^{(m)}$ and $\phi_{\beta}^{(m)}$. By assuming

$$\phi_{\beta}^{(m)} = \sum_{l=1}^{M_b} \phi_{\beta}^{(m,l)}, \tag{11}$$

with the corresponding modal amplitudes given by $B_{pq}^{(m)} = \sum_{l=1}^{M_b} B_{pq}^{(m,l)}$, the identification of the quantities of order m in Eq. (4) gives

$$\begin{aligned}
\left[\frac{\partial \phi_{\beta}^{(m)}}{\partial z}\right]_{z=-h_0} &= \sum_{l=1}^{M_b} \left(\frac{\partial \phi_{\beta}^{(m,l)}}{\partial z}\right)_{z=-h_0} \\
&= \sum_{l=1}^{M_b} \frac{\partial}{\partial x}\left[\frac{\beta^l}{l!}\frac{\partial^{l-1}}{\partial z^{l-1}}\left(\frac{\partial \phi_{h_0}^{(m)}}{\partial x}\right)\right]_{z=-h_0} + \sum_{l=1}^{M_b} \frac{\partial}{\partial y}\left[\frac{\beta^l}{l!}\frac{\partial^{l-1}}{\partial z^{l-1}}\left(\frac{\partial \phi_{h_0}^{(m)}}{\partial y}\right)\right]_{z=-h_0} \\
&\quad + \sum_{l=1}^{M_b}\sum_{j=1}^{l-1} \frac{\partial}{\partial x}\left[\frac{\beta^j}{j!}\frac{\partial^{j-1}}{\partial z^{j-1}}\left(\frac{\partial \phi_{\beta}^{(m,l-j)}}{\partial x}\right)\right]_{z=-h_0} \\
&\quad + \sum_{l=1}^{M_b}\sum_{j=1}^{l-1} \frac{\partial}{\partial y}\left[\frac{\beta^j}{j!}\frac{\partial^{j-1}}{\partial z^{j-1}}\left(\frac{\partial \phi_{\beta}^{(m,l-j)}}{\partial y}\right)\right]_{z=-h_0}.
\end{aligned} \tag{12}$$

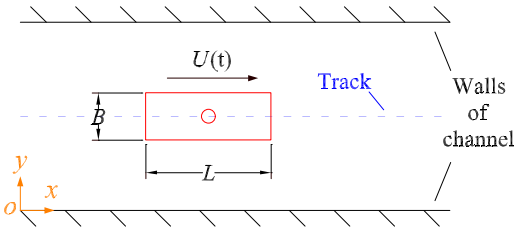

FIG. 1. Sketch of the present problem. The ship moves along the x direction on the centerline of the channel with a velocity $U(t)$. L, B, and d represent the length, width, and draft of the ship, respectively. The red rectangle denotes the ship, while the red circle denotes the center of the water plane, whose coordinates are (x^*, y^*).

Equation (12) with Eqs. (9) and (10) allows the computation of $B_{pq}^{(m)}(t)$ as a function of $A_{pq}^{(m)}(t)$. More specifically, $A_{pq}^{(m)}(t)$ is first computed based on Eqs. (2), (3), and (7), and $B_{pq}^{(m,1)}(t)$ is computed as a function of $A_{pq}^{(m)}(t)$. Then $B_{pq}^{(m,l)}(t)$ is computed as a function of $A_{pq}^{(m)}(t)$ and $B_{pq}^{(m,r)}(t)$ where $r = 1, 2, \ldots, l-1$ (see [28]).

We developed an in-house HOS-VB code with GPU acceleration for the present numerical simulations. To test the reliability of the proposed HOS-VB model, the results obtained using the fully nonlinear Boussinesq model (FUNWAVE-TVD), an open-source code developed by Shi *et al.* [29], are used for comparison. Furthermore, to study the nonlinear effects on mini-tsunamis, the results of these nonlinear models are compared with those obtained using the linear model developed by Grue [1].

III. SETUP FOR NUMERICAL SIMULATIONS

A. Moving pressure distribution

The length, width, and draft of the moving ship are denoted as L, B, and d, respectively (see Figs. 1 and 2). The advancing ship is simulated using a moving pressure distribution, p, which is defined as

$$p(x, y, t) = \rho g d f(x, t) q(y, t), \tag{13}$$

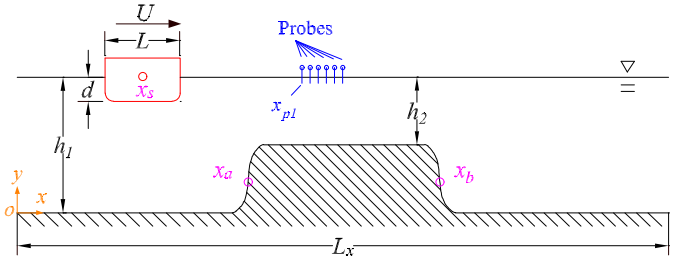

FIG. 2. Variable bathymetry, initial position of the ship x_s, and the positions of the six numerical wave probes along the x direction. h_1 and h_2 are the depths in the deep and relatively shallow regions, respectively. x_a and x_b are the two center positions of the depth changes. L and d denote the length and draft of the ship, respectively. U is the ship's velocity. x_{p1} is the position of the first numerical wave probe. The other five probes are placed every $1.25L$ along the x direction behind the first probe.

with

$$f(x,t) = \begin{cases} \cos^2\left[\frac{\pi\left(|x-x^*(t)|-\frac{1}{2}\alpha_s L\right)}{(1-\alpha_s)L}\right] & \frac{1}{2}\alpha_s L \leqslant |x-x^*(t)| \leqslant \frac{1}{2}L \\ 1 & |x-x^*(t)| \leqslant \frac{1}{2}\alpha_s L \end{cases}, \tag{14}$$

$$q(y,t) = \begin{cases} \cos^2\left[\frac{\pi\left(|y-y*(t)|-\frac{1}{2}\beta_s B\right)}{(1-\beta_s)B}\right] & \frac{1}{2}\beta_s B \leqslant |y-y^*(t)| \leqslant \frac{1}{2}B \\ 1 & |y-y^*(t)| \leqslant \frac{1}{2}\beta_s B \end{cases}. \tag{15}$$

The center of the water plane of the ship is located at (x^*, y^*), which is a function of time t. α_s and β_s are the coefficients that determine the shape of the wetted hull surface in the x and y directions, respectively [9,30]. If the static displacement of the ship V_0, along with the length, width, and draft of the ship, is determined, the values of α_s and β_s can be calculated based on $V_0 = \iint p/(\rho g d)\, dx\, dy$. The domain of the pressure distribution is the rectangular region defined by the ship's width and length, with the pressure being zero outside this region. In the present numerical simulations, $L/B = 4$, $\alpha_s = 0.4$, and $\beta_s = 0.2$ are used.

B. Moving velocity of a ship

In all cases considered in this study, the ship moves along the x direction on the centerline of the channel. As shown in Fig. 1, the two side walls are parallel to the moving track of the ship. The red rectangle denotes the ship, while the red circle denotes the center of the water plane of the ship, whose coordinates are (x^*, y^*). Only x^* varies with time, while y^* is kept unvaried. The variation in the moving velocity of the ship consists of two phases that can be defined as

$$U(t) = \begin{cases} U_0 \sin(t/T_a) & t/T_a \leqslant \frac{\pi}{2} \\ U_0 & t/T_a > \frac{\pi}{2} \end{cases}, \tag{16}$$

where T_a is a coefficient related to the acceleration duration, and U_0 is the steady moving velocity after the acceleration phase.

According to Eq. (16), $t/T_a \leqslant \pi/2$ is the gentle ramp up phase, where the velocity increases from 0 to U_0. The total distance for acceleration is $U_0 T_a$. In the present numerical simulations, $T_a/\sqrt{L/g} = 3.87$ is chosen.

When $t/T_a = \pi/2$, the velocity rises to U_0, and the ship then moves with the constant velocity U_0, which can be calculated based on Froude number. Note that the Froude number in the cases with variable bathymetry is defined as $\mathrm{Fr}_0 = U_0/\sqrt{g h_0}$, where h_0 is the average water depth.

C. Variable bathymetry

The bathymetry varies only in the along-channel direction and is uniform in the cross-channel direction. The change in depth in the along-channel direction is shown in Fig. 2. The depths in the deep and shallow regions are in nondimensional form, $h_1/L = 0.6$ and $h_2/L = 0.225$, respectively. Thus the depth difference Δh and average depth h_0 satisfy $\Delta h/L = 0.375$ and $h_0/L = 0.413$, respectively. The bottom is specified by $-h_0 + \beta(x)$, and the function of bathymetric variation $\beta(x)$ is defined as

$$\beta(x) = -\tfrac{1}{2}\Delta h_0 + \tfrac{1}{2}\Delta h_0\{\tanh[\gamma(x-x_a)] - \tanh[\gamma(x-x_b)]\}, \tag{17}$$

where the center positions of the two depth changes are at $x_a/L = 119.85$ and $x_b/L = 187.35$, respectively; γ is a parameter that controls the slope of the depth variation.

D. Test cases

Two types of channels with different widths are adopted to examine the influence of the channel width on the mini-tsunamis. For a narrow channel, the ratio of the channel width to the ship width

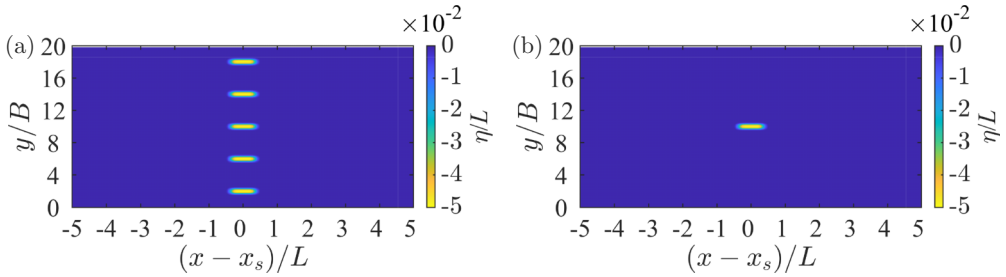

FIG. 3. Setup for the initial conditions of the numerical simulation. η is the surface elevation. L and B are the length and width of the ship, respectively. x_s is the position of the ship at $t = 0$. (a) Cases with narrow channel ($W/B = 4$); five identical ships are placed in parallel in the entire computational domain. Their moving velocities are the same. (b) Cases with a wide channel ($W/B = 20$); only one ship is placed in the entire computational domain.

is $W/B = 4$. To ensure the accuracy of computational results, a higher wave number resolution in the Fourier space which corresponds to a wider computational domain is required. Because periodic boundary conditions are used in the horizontal plane in HOS-VB and the ship travels along the centerline of the narrow channel, computational domain can be expanded by setting two ships which is symmetrical about wall of channel. In this way, the computational domain is twice as wide as the narrow channel. Following the same principle, computational domain can be further expanded, i.e., a computational domain whose width L_y is five times that of the narrow channel W is used in the present computation. The size of the total computational domain is set to $(L_x/L, L_y/B) = (307.2, 20)$, and the number of nodes is $(N_x, N_y) = (8192, 128)$. Because the entire computational domain is five times as wide as the ship ($L_y/W = 5$) and periodic boundary conditions are used in the horizontal plane, the total computational domain includes five narrow channels with the same width. Correspondingly, five identical ships are placed in parallel and travel along the x direction, which is shown in Fig. 3(a). The distance between two adjacent ships is equal to the width of the narrow channel, where the middle ship is placed along the centerline of the entire computational domain. The starting positions and velocities of these ships in the L_x direction are also the same. Because every two adjacent ships meet the symmetry principle regarding the centerline of their position, the centerline of each two adjacent ships' positions can be considered as a wall of narrow channel. Therefore, the situation of each ship shown in Fig. 3(a) is equivalent to a situation in which a ship travels along the centerline of a narrow channel with $W/B = 4$. However, compared to a computational domain with the same width as the narrow channel, the computational domain used in the present computation has a higher wave number resolution. For a wide channel, the ratio of the channel width to the ship width is $W/B = 20$. The size of the computational domain and the total number of nodes are the same as those in the case of a narrow channel. Because the width of the computational domain is equal to the width of a wide channel, only one ship is placed along the centerline of the computational domain. The total computational domain for a wide channel is shown in Fig. 3(b).

As illustrated in Fig. 2, the starting position of the ship in a nondimensional form is $x_s/L = 107.35$, and six numerical wave probes are placed along the centerline of the channel to record the shape of the mini-tsunamis. The first probe is fixed at $x_{p1}/L = 153$, while the others are placed every $1.25L$ after the first one along the x direction.

All the test cases are summarized in Table I. The letter in the name of each case is used to distinguish the different channel widths: "N" and "W" denote the narrow and wide channels, respectively. In Tests N01 to N04 and Tests W01 to W04, the results obtained with $\mathrm{Fr}_0 = 0.387$, 0.457, 0.527, and 0.562 are compared to analyze the influence of the Froude number. Moreover, different values of h_0/d, namely, 16.5, 8.25, 5.5, and 4.125, are used in Tests N02, N05, N06, and

TABLE I. Main parameters used in test cases in the present numerical simulation. W/B denotes the ratio of channel width to ship width, Fr_0 denotes the Froude number based on average depth, h_0/d is the ratio of average depth to ship draft, and γ is the slope of the depth variation.

Test	W/B	Fr_0	h_0/d	γ
N01	4	0.387	8.250	1.167
N02	4	0.457	8.250	1.167
N03	4	0.527	8.250	1.167
N04	4	0.562	8.250	1.167
N05	4	0.457	16.500	1.167
N06	4	0.457	5.500	1.167
N07	4	0.457	4.125	1.167
N08	4	0.457	8.250	0.500
N09	4	0.457	8.250	0.833
N10	4	0.457	8.250	1.500
W01	20	0.387	8.250	1.167
W02	20	0.457	8.250	1.167
W03	20	0.527	8.250	1.167
W04	20	0.562	8.250	1.167
W05	20	0.457	16.500	1.167
W06	20	0.457	5.500	1.167
W07	20	0.457	4.125	1.167
W08	20	0.457	8.250	0.500
W09	20	0.457	8.250	0.833
W10	20	0.457	8.250	1.500

N07 and Tests W02, W05, W06, and W07 to investigate the influence of the ratio between average water depth and ship draft on the mini-tsunamis. Furthermore, because the bathymetric variation contributes to the generation of mini-tsunamis, $\gamma = 0.5$, 0.833, 1.167 and 1.5 are chosen in Tests N02, N08, N09, and N10 and Tests W02, W08, W09, and W10 to examine the impact of the slope of the depth variation on the mini-tsunamis.

IV. VALIDATION OF THE PRESENT NUMERICAL MODEL

A. Comparison with experiment in a tank with a flat bottom

To investigate upstream solitary waves induced by a moving ship, Ertekin *et al.* [12] conducted experiments in the Ship Model Towing Tank of the University of California, Berkeley. The tank with a flat bottom has a length of 61 m and a width of 1.22 m. The water depth is 0.125 m. In the experiment, a Series 60 ship with a block coefficient $C_B = 0.8$ is used. The length, width, and draft of the ship model are 1.524 m, 0.234 m, and 0.075 m, respectively. The ship which is rigidly attached to an aluminum truss below the towing carriage starts from rest and moves along the centerline of the tank at a Froude number $\mathrm{Fr} = 0.8$. To record upstream waves, a wave probe is placed on the centerline of tank. The position of the wave probe is 3.86 m ahead of the initial position of the ship. To validate the present numerical model, we simulate the experiment using HOS-VB with a nonlinear order of $M = 3$. The numerical wave probe is placed at the same position as that in the experiment. The computed wave elevation is compared with the experimental data, as illustrated in Fig. 4. As can be observed, the short waves with gradually decreasing amplitude propagate behind the main leading wave. The amplitudes and phases of the leading wave and the short waves computed by HOS-VB ($M = 3$) agree well with the measurements in the experiment. Moreover, the mean free-surface levels of these upstream waves in the numerical and experimental results agree well and are approximately 0.014 m.

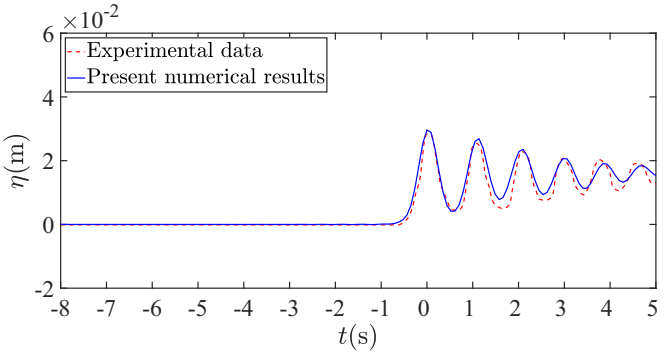

FIG. 4. Comparison of the numerical wave probe records computed using HOS-VB ($M = 3$) and the experimental gauge records obtained by Ertekin *et al.* [12]. A Series 60 ship with block coefficient $C_B = 0.8$ is used in experiments. The length, width, and draft of the model ship are 1.524 m, 0.234 m, and 0.075 m, respectively. The ship model starts from rest and moves along the centerline of the tank with a Froude number Fr = 0.8. The width of the tank is 1.22 m. The water depth is 0.125 m. The gauge in the experiment and the numerical wave probe are placed along the centerline of the tank. In the numerical simulations, the water depth is set to the same depth as in the experiment with depth variation parameter $\beta = 0$.

B. Comparison with field measurements collected by a wave radar

In 2009, to study the mini-tsunamis, a wave radar was installed on the shore at Flaskebekk Pier, near Ildjernsflu, Oslofjorden, Norway. The wave radar records were reported in Grue *et al.* [23]. To validate the proposed model with variable bathymetry, we simulate the same phenomenon using HOS-VB with different nonlinear orders and compare the results with the radar measurements and the linear results.

Because the ship's route is parallel to the shore at a distance of 1.2 km, a channel with a width of 2.4 km is used in the simulation, where the ship cruises along the centerline of the channel. The length, width, and draft of the ship are 210 m, 35 m, and 6.8 m, respectively. The shallow region of Ildjernsflu extends approximately 700 m along the route of the ship, and the depth of the shallowest region is approximately 14 m. The depth before and after the shallow region is approximately 46 m. Therefore, the average water depth $h_0 = (14 + 46)/2 = 30$ m is comparable to the depth change $\Delta h = 46 - 14 = 32$ m. The Froude number based on the average depth is 0.583 in the test case. Although the bottom near Ildjernsflu is quite uneven in the shallow region, an approximated depth profile can be represented in Eq. (17) [23].

Figure 5 shows the comparison of the present numerical results with the measurements by a wave radar. As can be observed, the elevation at approximately $t = -15$ s denotes the main wave generated by the depth change; the main trough is placed at $t = 0$ in the plots. The solid magenta line denotes the results computed using the linear model. The results from HOS-VB ($M = 1$, $M_b = 2$), represented by the blue dashed line, compare well with the solutions obtained using the linear model. This is expected as shown in Appendix B that these two models are comparable. However, the crest height of the main wave in the linear model is significantly lower than that obtained by the radar measurements. Considering the bottom and free-surface nonlinearities, we simulate the test case using HOS-VB ($M = 3$, $M_b = 5$), which is denoted by the red dashed line. Comparing the nonlinear and linear results with the radar data, we find that HOS-VB ($M = 3$, $M_b = 5$) is more accurate in terms of the main wave crest and trough. In addition, several short waves following the main wave recorded by the radar can also be captured by HOS-VB ($M = 3$, $M_b = 5$), but these waves are not present in the results obtained using the linear model. The waves at approximately $t = -50$ s in the radar data are not observed in the numerical models, and the phase of the main wave in the radar measurement is somewhat different from that in the results computed by the linear model and HOS-VB, which could be attributed to the idealization of the bathymetry.

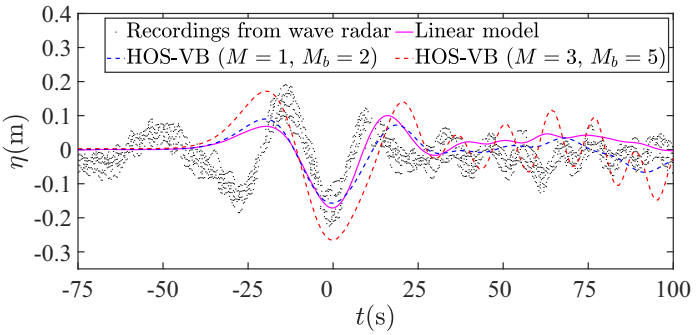

FIG. 5. Comparison of the present numerical results with the measurements collected by a wave radar. The black dots represent the wave elevation measured by the wave radar for eight passages of the ship, Color Fantasy. Fr_0 ranges from 0.556 to 0.589. The magenta solid line is the results computed by the linear model proposed by Grue *et al.* [23]. Results obtained using HOS-VB ($M = 1, M_b = 2$) and HOS-VB ($M = 3, M_b = 5$) are denoted by the blue and red dashed line, respectively.

The water depth used for numerical simulation is an estimation from the water depth along the ship's track, but is uniform in the cross-channel direction. However, the water depth in reality is quite uneven and gradually decreases from the ship's track to the shore. Therefore, the position near the shore where the time series of waves are recorded has a smaller water depth in reality than that in numerical simulation, and the main wave recorded by the wave radar has a different dispersion relation from that in numerical simulation as the wave propagates from the ship's track to the shore. This difference in dispersion relation might cause the phase difference.

In summary, by comparison with the radar records, HOS-VB ($M = 3$, $M_b = 5$) shows better accuracy than the linear model in the simulation of mini-tsunamis and the short waves behind.

V. GENERATION AND PROPAGATION OF MINI-TSUNAMIS

Mini-tsunamis are generated when a ship travels from deep to shallow water at subcritical speeds. The generation mechanism can be explained in Fig. 6 (see Grue *et al.* [23]). The normal velocity of the water at a depth decrease (denoted by arrow 1) is induced by the arrival of the ship's bow, producing a reaction velocity at the bottom (arrow 2). The reaction velocity appears as a vertical velocity on the free surface (arrow 3), which generates the mini-tsunamis.

To analyze the generation of mini-tsunamis, Tests N02 and W02 are selected for the numerical simulations. In these two cases, a ship moves from the deep to shallow water at a subcritical speed through the narrow ($W/B = 4$) and wide channels ($W/B = 20$), respectively. Except for the channel width, the other parameters in these two cases are the same. The depth difference Δh and average depth h_0 satisfy $\Delta h/L = 0.375$ and $h_0/L = 0.413$, respectively. The slope coefficient of the depth

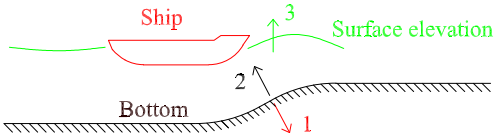

FIG. 6. Interaction of a ship's bow and the variable bottom as the ship travels from deep to shallow water. The black, red, and green lines represent the bottom, the ship and the surface elevations, respectively. The normal velocity of the fluid on the variable bottom is induced by the bow (arrow 1), and then a reaction velocity (arrow 2) is produced by the impenetrable bottom. The reaction velocity finally appears as an upward velocity (arrow 3), which results in the free-surface elevation.

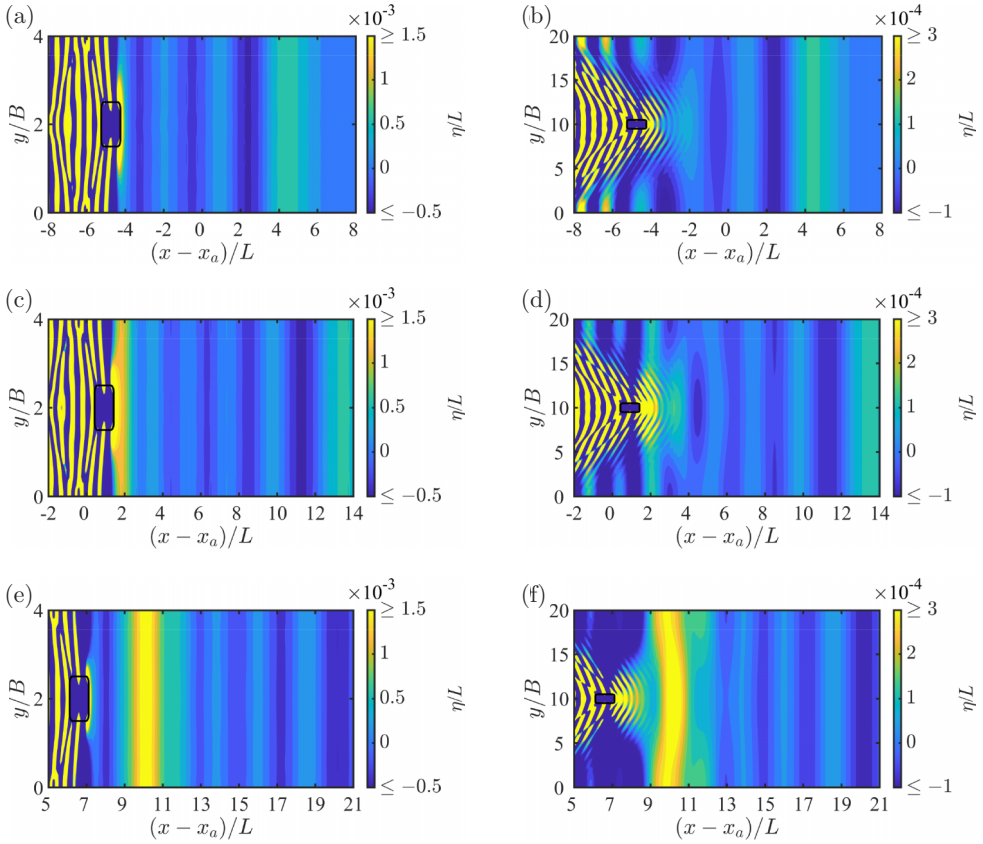

FIG. 7. The three plots on the left that are about the surface elevation η at (a) $t/\sqrt{L/g} = 1162$, (c) $t/\sqrt{L/g} = 1936$ and (e) $t/\sqrt{L/g} = 2711$ show the generation process of mini-tsunamis in the narrow channel (Test N02). The three plots on the right that are about the surface elevation η at (b) $t/\sqrt{L/g} = 1162$, (d) $t/\sqrt{L/g} = 1936$, and (f) $t/\sqrt{L/g} = 2711$ show the generation process of mini-tsunamis in the wide channel (Test W02). x_a, denoted in Fig. 2, is the center position of the depth change.

variation γ is 1.167. The ratio of the length to the width of the ship is $L/B = 4$, and the ratio of the average depth to the draft of the ship is $h_0/d = 8.25$. In addition, the Froude number is $\mathrm{Fr}_0 = 0.457$, and the nondimensional time related to the initial acceleration is $T_a/\sqrt{L/g} = 3.87$.

The three snapshots presented on the left and right sides of Fig. 7 show a ship traveling from deep to shallow water in the narrow and wide channels, respectively. In the case with the narrow channel, Fig. 7(a) shows a time before the ship arrives at the depth change. At approximately $(x - x_a)/L = 5$, the light green band parallel to the cross-channel direction represents the waves produced by the ship accelerating in deep water. Figure 7(c) shows the moment when the ship has just passed the depth change location x_a. Compared with Fig. 7(a), in Fig. 7(c), the surface elevation at the bow is more significant, indicating the ship-driven mini-tsunamis. However, the mini-tsunamis and the bow are not separated. At this time, the waves induced by the initial acceleration of the ship arrive at approximately $(x - x_a)/L = 14$. Figure 7(e) shows the time when the mini-tsunamis are fully developed and travel ahead of the ship in the shallow-water region. The mini-tsunamis can be observed as the bright band located at $(x - x_a)/L = 9$ to 12.5. The yellow band at approximately $(x - x_a)/L = 10.5$ represents the region near the wave crest where the amplitude is large. In addition, the reflection of the wake waves owing to the vertical walls of the channel is evident. Although the generation process of mini-tsunamis in the wide channel shown in Figs. 7(b), 7(d),

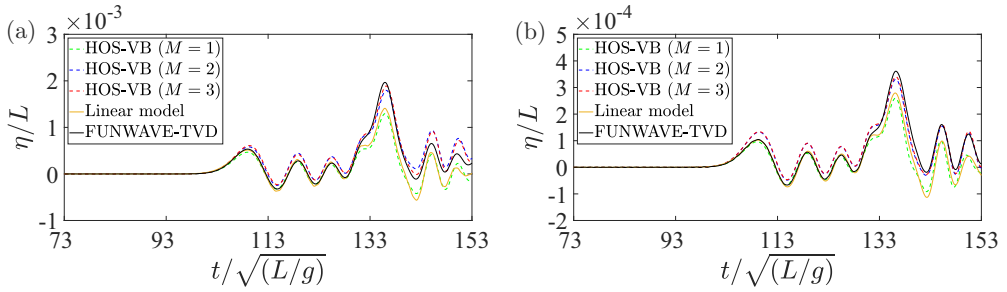

FIG. 8. Wave records from the fourth numerical wave probes at $x_{p4} = 156.75L$ in the (a) narrow channel with a width of $W/B = 4$ (Test N02) and the (b) wide channel with a width of $W/B = 20$ (Test W02). $t/\sqrt{L/g}$ is the nondimensional time. The surface elevation η is computed by different models. The order of bottom nonlinearity is $M_b = 5$, and different orders of free-surface nonlinearity M are adopted in HOS-VB.

and 7(f) is similar to that in the narrow channel, there are some differences in the crestlines. As can be seen in the figure, the crestline is curved in the wide channel in contrast to a straight line in the narrow channel.

The wave records from the fourth numerical wave probe at $x_{p4} = 156.75L$ are shown in Fig. 8. The results obtained using the linear model, fully nonlinear model FUNWAVE-TVD, and HOS-VB with different nonlinear orders of the free surface are compared. In the narrow or wide channel, the first wave followed by two short waves is generated by the ship accelerating from rest in the deep region. In each plot, the fourth wave with the largest amplitude denotes a mini-tsunami generated by the depth change. As can be observed, the amplitude of the mini-tsunami in the wide channel is much less than that in the narrow channel. The wave amplitudes of mini-tsunamis obtained using the linear model and HOS-VB ($M = 1$) are almost the same. The wave amplitude computed by HOS-VB ($M = 2$), which is higher than the linear results, is close to that in HOS-VB ($M = 3$). This suggests that the second-order nonlinearity plays a significant role in increasing the wave amplitude of the mini-tsunamis, whereas the contribution of the third-order nonlinearity is minor. Moreover, the results obtained using FUNWAVE-TVD agree relatively well with those computed using HOS-VB ($M = 3$), which shows the reliability of the HOS-VB model.

Furthermore, the mini-tsunamis are followed by several short waves. The mean free-surface level of these short waves is significant in the cases with a narrow channel and a high Froude number, such as Test N04 shown in Fig. 9. The mean free-surface level of these short waves is nearly zero

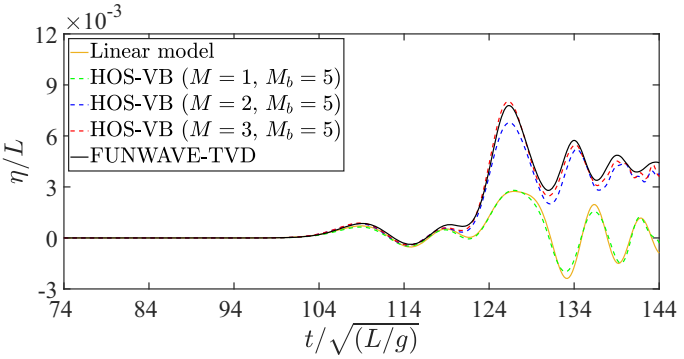

FIG. 9. Wave records from the fourth numerical wave probes at $x_{p4} = 156.75L$ in Test N04. The width of the channel in a nondimensional form is $W/B = 4$, and the Froude number based on the average depth is $\mathrm{Fr}_0 = 0.562$. The mean free-surface level of short waves propagating behind mini-tsunamis is nearly zero in the linear model, but is significantly elevated above zero in higher-order nonlinear models: HOS-VB ($M = 2$), HOS-VB ($M = 3$), and FUNWAVE-TVD.

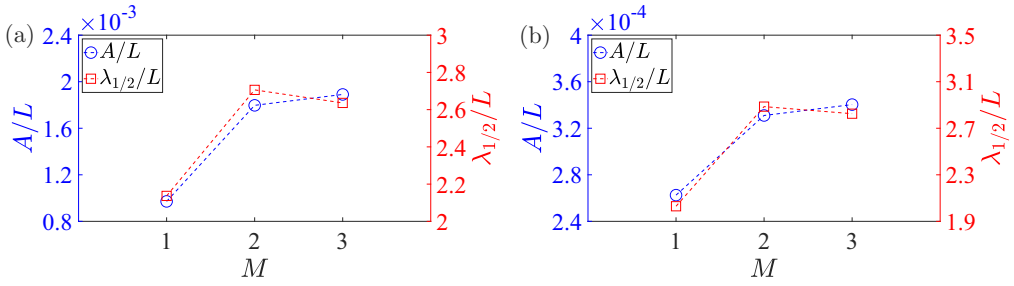

FIG. 10. Comparison of the wave amplitude A and wavelength at half-crest height $\lambda_{1/2}$ computed by the HOS-VB ($M_b = 5$) with different free-surface nonlinear order M. The blue circle represents the nondimensional amplitude A/L, which is plotted against the blue vertical axis on the left side. Red square represents the nondimensional wavelength at half-crest height $\lambda_{1/2}/L$ which is plotted against the red vertical axis on the right side. (a) Narrow channel with a width of $W/B = 4$ (Test N02). (b) Wide channel with a width of $W/B = 20$ (Test W02).

in the linear model and HOS-VB ($M = 1$). But, in the higher-order models, this is significantly higher than the calm water level $z = 0$. This indicates that the increase in the mean free-surface level, similar to that of the bore ahead of the bow, is a nonlinear phenomenon. By comparing the results obtained using HOS-VB with different orders of free-surface nonlinearity M, the increase in the mean free-surface level is primarily attributed to the second-order nonlinearities.

Comparison of the amplitude A and wavelength at half-crest height $\lambda_{1/2}$ of mini-tsunamis computed by HOS-VB with different nonlinear orders M in the narrow and wide channels is illustrated in Fig. 10. As can be observed, higher-order nonlinearities contribute not only to an increase in the wave amplitude but also to an increase in the wavelength. The wave amplitudes in the narrow channel are larger than those in the wide channel. However, the wavelengths at the half-crest height computed using HOS-VB with $M = 2$ and $M = 3$ are hardly affected by the channel width. In the narrow and wide channels, the wavelength at half-crest height obtained using HOS-VB with $M = 3$ is approximately 2.7 times as long as the length of ship.

To investigate the properties of the mini-tsunamis in the narrow and wide channels, the wave elevation obtained from six numerical wave probes placed along the centerline are shown in Fig. 11. The position of the first probe in the x direction is $x_{p1} = 153L$, which is $33.15L$ away from the center position of the depth change at x_a. The first to the last probe records are shown in order from the

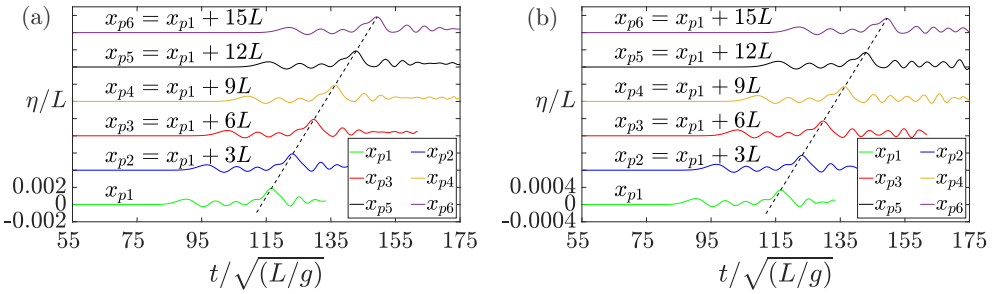

FIG. 11. Wave records of six numerical wave probes in the (a) narrow channel with a width of $W/B = 4$ (Test N02) and the (b) the wide channel with a width of $W/B = 20$ (Test W02) computed by HOS-VB ($M = 3$, $M_b = 5$). The position of the first probe is $x_{p1} = 153L$, while the positions of the other five probes are denoted as x_{p2}, x_{p3}, x_{p4}, x_{p5}, and x_{p6}, respectively. The distance between two adjacent probes in the x direction is $3L$. The solid lines with different colours represent six probe records at different positions, and the black dashed line is fitted for the propagation of the crests of the mini-tsunamis.

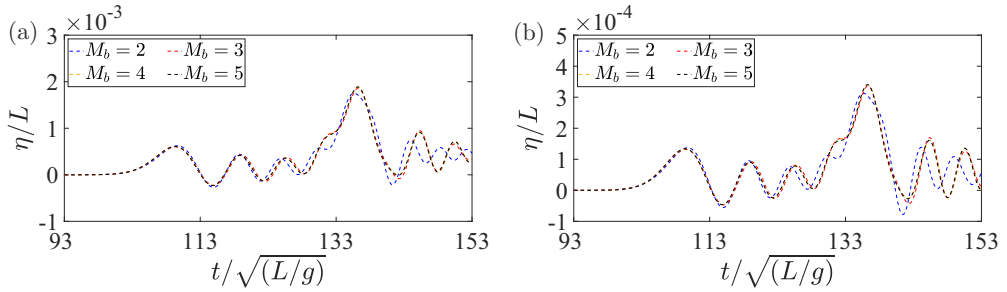

FIG. 12. Effects of bottom nonlinearities in the (a) narrow channel with a width of $W/B = 4$ (Test N02) and the (b) wide channel with a width of $W/B = 20$ (Test W02). Free surface elevation η is recorded by the fourth numerical wave probe at $x_{p4} = 156.75L$. Results are computed using the HOS-VB ($M = 3$) with different orders of bottom nonlinearities M_b.

bottom to the top of the plot. In each probe record, the fourth wave with the largest amplitude denotes a mini-tsunami and is followed by a number of short waves with small amplitudes. In the narrow channel, the amplitude of the short waves behind the mini-tsunami decreases as the distance between the short wave and the mini-tsunami increases. However, this attenuation is not significant in the wide channel.

To compute the phase velocity, we fit a black dashed line for the propagation of the crest of the mini-tsunamis in each channel. The phase velocity is approximately $0.97\sqrt{gh_2}$ in both channels and is thus not significantly affected by the channel width.

VI. EFFECTS OF BOTTOM AND FREE-SURFACE NONLINEARITIES ON MINI-TSUNAMIS

A. Effects of bottom nonlinearities

In HOS-VB, M_b and M represent the nonlinear orders of the variable topography and free surface, respectively. To test the influence of bottom nonlinearities on the properties of mini-tsunamis, different orders of bottom nonlinearity, that is, $M_b = 2$, 3, 4, and 5, are adopted. M is set to 3, which means that third-order free-surface nonlinearities are included.

The wave records of the fourth numerical wave probe at $x_{p4} = 156.75L$ in the narrow and wide channels are shown in Fig. 12. In each wave record, the fourth wave with the largest wave amplitude denotes a mini-tsunami generated by the depth change. Good convergence of the wave form of the mini-tsunamis is shown by the results for $M_b = 2$, 3, 4, and 5. The nonlinear effects of the variable topography on the wave amplitude, wavelength at half-crest height, and phase velocity are discussed below.

1. Effects of bottom nonlinearities on wave amplitude

The variation of amplitude A and wavelength at half-crest height $\lambda_{1/2}$ of mini-tsunamis with respect to the order of bottom nonlinearity M_b is shown in Fig. 13. As can be seen, in both the narrow and wide channels, the amplitude converges with M_b and is enhanced by the high-order nonlinearities of the variable bottom, particularly by the third-order nonlinearities. The increment between the values of A/L for $M_b = 2$ and $M_b = 3$ is about 10%. However, the increase in A/L is negligible as M_b varies from 3 to 5.

2. Effects of bottom nonlinearities on wavelength at half-crest height

As illustrated in Fig. 13, the wavelength at half-crest $\lambda_{1/2}$ barely changes as the order of nonlinearity on the bottom M_b increases. As M_b varies from 2 to 5, in the narrow channel, the wavelength at the half-crest height is approximately 1.7 times the length of the ship, while in

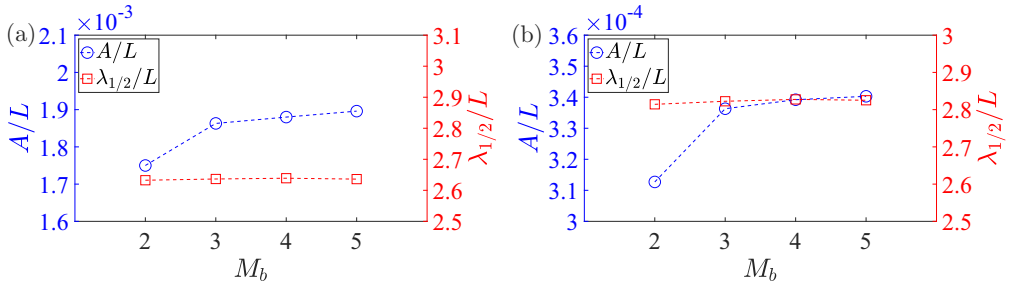

FIG. 13. Comparison of the amplitude A and wavelength at half-crest height $\lambda_{1/2}$ obtained using the HOS-VB ($M = 3$) with different bottom nonlinear orders of M_b. The blue circle represents the nondimensional amplitude A/L, which is plotted against the blue vertical axis on the left side. The red square represents the nondimensional wavelength at half-crest height $\lambda_{1/2}/L$, which is plotted against the red vertical axis on the right side. (a) Results in the narrow channel with a width of $W/B = 4$ (Test N02). (b) Results in the wide channel with a width of $W/B = 20$ (Test W02).

the wide channel, it is approximately 2.82 times the length of the ship. This suggests that the higher-order nonlinearities from a variable topography have little influence on the wavelength at half-crest height.

3. Effects of bottom nonlinearities on phase velocity

In the shallow water, six numerical wave probes are placed along the centerline of the channel to compute the phase velocity of the mini-tsunamis. As shown in Fig. 14, among the cases with different M_b, the phase velocities are almost the same. Specifically, the phase velocity ranges from $0.961\sqrt{gh_2}$ to $0.978\sqrt{gh_2}$ where h_2 is the shallow-water depth. It suggests that the channel width and the bottom nonlinearities have no significant effect on the phase velocity of mini-tsunamis.

B. Effects of free-surface nonlinearities

To investigate the effects of free-surface nonlinearities on mini-tsunamis, we use $M_b = 5$, which is sufficient for considering the bottom nonlinearities. The results obtained using the linear model and HOS-VB with different orders of free-surface nonlinearity M are compared.

First, the influence of the free-surface nonlinearities in the test cases with different Froude numbers based on the average water depth, that is, $\mathrm{Fr}_0 = 0.387$, 0.457, 0.527, and 0.562, is studied,

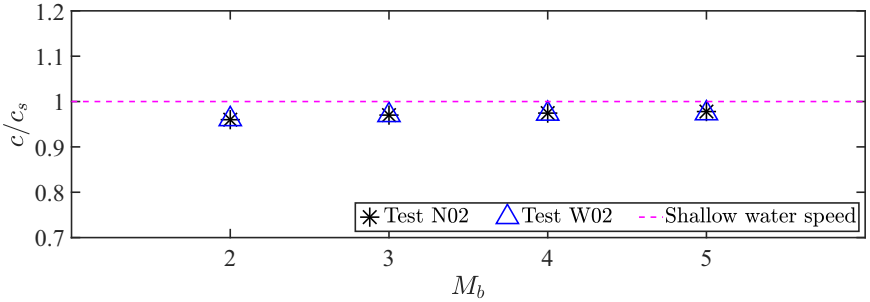

FIG. 14. Comparison of the phase velocity c of mini-tsunamis obtained using the HOS-VB ($M = 3$) with different bottom nonlinear orders of M_b. The shallow-water speed is $c_s = \sqrt{gh_2}$ where h_2 is the shallow-water depth. The black asterisks represent the results in the narrow channel (Test N02). The blue triangles represent the results in the wide channel (Test W02).

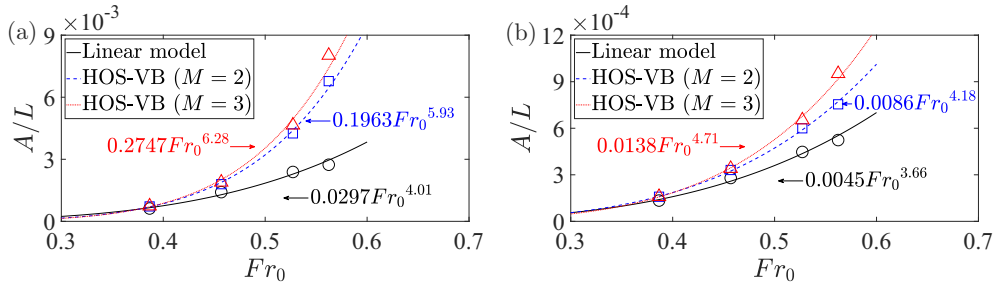

FIG. 15. Influence of free-surface nonlinearities on the amplitudes A of mini-tsunamis in cases with different Froude numbers based on the average water depth, that is, $\mathrm{Fr}_0 = 0.387$, 0.457, 0.527, and 0.562. (a) Narrow channel with a width of $W/B = 4$. (b) Wide channel with a width of $W/B = 20$.

corresponding to Tests N01 to N04 and Tests W01 to W04 for the narrow and wide channels, respectively. Second, the free-surface nonlinearities under different ratios of the average depth to the draft of ship, namely, $h_0/d = 16.5$, 8.25, 5.5, and 4.125, in the narrow (Tests N02, N05, N06, and N07) and wide channels (Tests W02, W05, W06, and W07), are investigated. In addition, because the variable bathymetry is a key factor in the generation of mini-tsunamis, the slope of the depth variation γ is expected to be a key parameter. To study the influence of bottom slope on free-surface nonlinearities, $\gamma = 0.5$, 0.833, 1.167, and 1.5 are chosen in Tests N02, N08, N09, and N10 conducted for the narrow channel and Tests W02, W08, W09, and W10 conducted for the wide channel.

In the above mentioned test cases, for example, as shown in Fig. 8, the wave forms of the mini-tsunamis computed by the linear model and HOS-VB ($M = 1$, $M_b = 5$) are approximately the same. Therefore, the differences between the results obtained using HOS-VB ($M = 2$, $M_b = 5$), HOS-VB ($M = 3$, $M_b = 5$), and the linear model are primarily caused by the free-surface nonlinearities, whereas the high-order bottom effects are negligible. The impact of free-surface nonlinearities on the amplitude, wavelength at half-crest height, and phase velocity of mini-tsunamis in different cases is analyzed as follows.

1. Effects of free-surface nonlinearities on wave amplitude

Based on the cases in which different Fr_0 are adopted (Tests N01 to N04 and Tests W01 to W04), Fig. 15 shows that under the same Froude number Fr_0, the amplitude in the narrow channel is larger than that in the wide channel, and that the amplitude of the mini-tsunami grows with Fr_0. This increasing trend can be explained by the generation mechanism of mini-tsunamis, as illustrated in Fig. 6. The fast moving ship can induce a high reaction velocity on the depth change (arrow 2) and a considerable normal velocity on the free surface (arrow 3), which results in a larger amplitude of upstream wave. Furthermore, based on the results computed using different models, the fitted curves corresponding to Fr_0^{α} are obtained and plotted in Fig. 15. The value of α ranges from 3.7 to 4.0 in the linear model but varies from 4.2 to 6.3 in the high-order nonlinear models. The larger the value of α, the faster the amplitude of the mini-tsunami increases with respect to Fr_0. Therefore, in both the narrow and wide channels, the largest growth rate is observed in HOS-VB ($M = 3$, $M_b = 5$), which is slightly larger than that in HOS-VB ($M = 2$, $M_b = 5$), whereas the smallest growth rate is observed in the linear model. This indicates that the higher-order free-surface nonlinearities contribute to the increase in the amplitude of the mini-tsunami. Second-order free-surface nonlinearities provide the most significant contribution, and the effects of the third-order free-surface nonlinearities are enhanced as Fr_0 rises. In addition, the variation in the wave amplitude in the narrow channel is more sensitive to Fr_0 than that in the wide channel.

TABLE II. Values of ε_{12}, ε_{13}, and ε_{23} for all the cases with depth change in the narrow channel with $W/B = 4$.

Test	Fr	h/d	γ	ε_{12}	ε_{13}	ε_{23}
N01	0.387	8.250	1.167	16.14%	18.97%	2.44%
N02	0.457			27.27%	33.85%	5.18%
N03	0.527			78.13%	94.76%	9.34%
N04	0.562			147.64%	193.09%	18.35%
N05	0.457	16.500	1.167	19.78%	21.07%	1.08%
N02		8.250		27.27%	33.85%	5.18%
N06		5.500		50.91%	71.51%	13.65%
N07		4.125		57.45%	108.60%	32.48%
N08	0.457	8.250	0.500	52.46%	56.75%	2.82%
N09			0.833	40.83%	47.03%	4.40%
N02			1.167	27.27%	33.85%	5.18%
N10			1.500	35.61%	43.26%	5.64%

To quantify the influence of higher-order free-surface nonlinearities on the amplitude of the mini-tsunami, three nondimensional parameters are defined as

$$\varepsilon_{12} = |\tilde{A}_2 - \tilde{A}_1|/\tilde{A}_1, \tag{18}$$

$$\varepsilon_{13} = |\tilde{A}_3 - \tilde{A}_1|/\tilde{A}_1, \tag{19}$$

$$\varepsilon_{23} = |\tilde{A}_3 - \tilde{A}_2|/\tilde{A}_2, \tag{20}$$

where $\tilde{A}_1$, $\tilde{A}_2$, and $\tilde{A}_3$ denote the nondimensional wave amplitudes A/L obtained using the linear model, HOS-VB ($M = 2$, $M_b = 5$), and HOS-VB ($M = 3$, $M_b = 5$), respectively. Therefore, ε_{12} is defined to measure the effects of the second-order free-surface nonlinearities, ε_{13} is adopted to quantify the influence where both of the second- and third-order free-surface nonlinearities are included, and ε_{23} is used to evaluate the effects of the third-order free-surface nonlinearities.

To quantify nonlinear free-surface effects under different conditions with respect to Fr_0, the values of ε_{12}, ε_{13}, and ε_{23} in all the cases with a narrow channel and a wide channel are listed in Tables II and III, respectively. As can be observed, all of the three parameters increase with Fr_0, which

TABLE III. Values of ε_{12}, ε_{13} and ε_{23} for all the cases with depth change in the wide channel with a width of $W/B = 20$.

Test	Fr	h/d	γ	ε_{12}	ε_{13}	ε_{23}
W01	0.387	8.250	1.167	18.43%	18.96%	0.44%
W02	0.457			18.43%	21.75%	2.81%
W03	0.527			34.02%	45.95%	8.91%
W04	0.562			44.00%	81.66%	26.15%
W05	0.457	16.500	1.167	12.49%	13.27%	0.69%
W02		8.250		18.43%	21.75%	2.81%
W06		5.500		39.39%	48.12%	6.27%
W07		4.125		48.96%	65.73%	11.26%
W08	0.457	8.250	0.500	35.14%	38.71%	2.64%
W09			0.833	29.73%	33.29%	2.74%
W02			1.167	18.43%	21.75%	2.81%
W10			1.500	26.35%	29.95%	2.85%

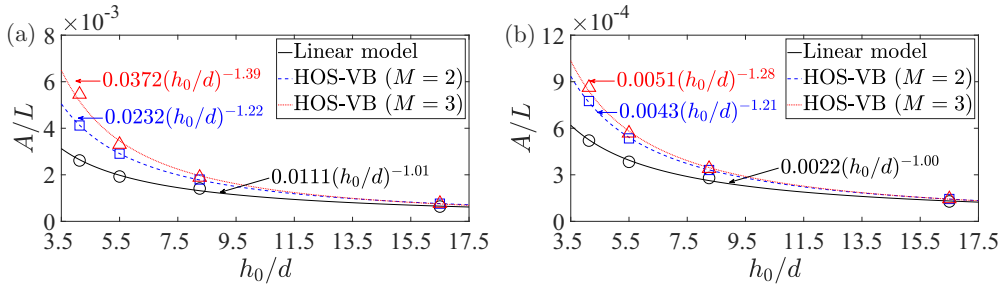

FIG. 16. Influence of free-surface nonlinearities on the amplitudes A of mini-tsunamis in cases with different ratios of average water depth to the draft of ship, namely, $h_0/d = 16.5, 8.25, 5.5$, and 4.125. (a) Results in the narrow channel with a width of $W/B = 4$. (b) Results in the wide channel with a width of $W/B = 20$.

corresponds to the fitted curves presented in Fig. 15. When $\mathrm{Fr}_0 = 0.562$, ε_{13} can reach 193.09% and 81.66% in the narrow and wide channels, respectively. This implies that the influence of the second- and third-order free-surface nonlinear effects is prominent when the Froude number is high. Comparing the difference between ε_{13} and ε_{12}, we can observe that the most important contribution comes from second-order free-surface nonlinearities, which are even able to increase the amplitude by approximately 147.64% when $\mathrm{Fr}_0 = 0.562$ in the narrow channel. The third-order free-surface nonlinearities are negligible when Fr_0 is small. However, the gradual increase in ε_{23} indicates the third-order free-surface nonlinearities tend to be enhanced as the ship speed increases.

Figure 16 shows the wave amplitudes of the mini-tsunamis in the cases where different ratios of the average depth to the draft of ship h_0/d are adopted (Tests N02, N05, N06, and N07 and Tests W02, W05, W06, and W07). The wave amplitude varies inversely with h_0/d in both the narrow and wide channels. This tendency can be explained from Fig. 6. If the bottom and the velocity of the ship are assumed to be unvaried, a large ratio of average depth to ship draft h_0/d implies a small distance between the ship and the sea bottom. Therefore, the water velocity generated by the moving ship has little attenuation from bow to seafloor, which results in a high reaction velocity on the seafloor (arrow 2) and a considerable normal velocity on the free surface (arrow 3), causing a large mini-tsunami.

Based on the fitted curves corresponding to $(h_0/d)^\alpha$ depicted in Fig. 16 and the values of ε_{12}, ε_{13} and ε_{23} presented in Tables II and III, the free-surface nonlinear effects on the amplitude of mini-tsunami under the cases with different ratios of average depth to ship draft h_0/d are discussed. The absolute value of α, which denotes the decreasing rate of A/L with h_0/d, is about 1 in the linear model but ranges from 1.2 to 1.4 in the high-order nonlinear models. The absolute value of α in HOS-VB ($M = 3$, $M_b = 5$) is higher than that in the linear model or HOS-VB ($M = 2$, $M_b = 5$), demonstrating that the amplitude increase resulting from the second- and third-order free-surface nonlinearities becomes more significant when h_0/d is smaller. For example, when $h_0/d = 4.125$, the wave amplitude computed by HOS-VB ($M = 3, M_b = 5$) is more than twice the wave amplitude computed by the linear model in the narrow channel, $\varepsilon_{13} = 108.60\%$. However, the three fitted curves depicted in Fig. 16 nearly coincide in the regions of $h_0/d > 16.5$, which illustrates that the higher-order nonlinearities are nearly negligible when h_0/d is large. Furthermore, the increase of the wave amplitude primarily depends on the second-order free-surface nonlinearities which can even boost the amplitude by 57.45% at $h_0/d = 4.125$ in the narrow channel. Although the third-order nonlinearities are not as evident as the second-order nonlinearities, they are enhanced as the ratio of average depth to ship draft h_0/d declines; accordingly, ε_{23} can reach 32.48% at $h_0/d = 4.125$ in the narrow channel.

The free-surface nonlinear effects under the conditions with different slopes of the depth change γ (Tests N02, N08, N09, and N10 and Tests W02, W08, W09, and W10) are studied. A larger value of γ represents a steeper slope. Figure 17 shows that the wave amplitude A increases with the

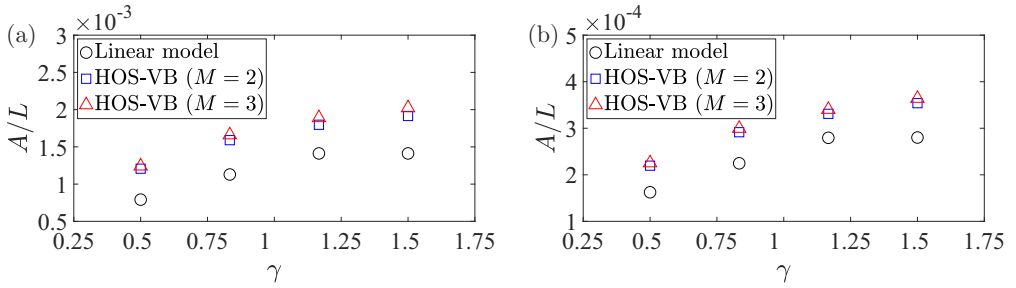

FIG. 17. Influence of free-surface nonlinearities on the amplitudes A of mini-tsunamis in cases with different slopes of the depth change, namely, $\gamma = 0.5$, 0.833, 1.167, and 1.5. (a) Results in the narrow channel with a width of $W/B = 4$. (b) Results in the wide channel with a width of $W/B = 20$.

slope of the bottom variation. But the growth rate tends to decrease as $\gamma > 1.167$. As also shown in Tables II and III, when the slope of the bottom variation γ varies from 0.5 to 1.167, the second-order free-surface nonlinear effects (denoted by ε_{12}) and the effects including both second- and third-order nonlinearities (denoted by ε_{13}) decline with γ. However, when the slope of the bottom variation γ ranges from 1.167 to 1.5, the second-order free-surface nonlinear effects (denoted by ε_{12}) and the effects including both of the second- and third-order nonlinearities (denoted by ε_{13}) increase with γ. In addition, based on the variation of ε_{23} with γ shown in the tables, it is found that the increase of the third-order free-surface nonlinear effects in both narrow and wide channels is not significant.

2. Effects of free-surface nonlinearities on wavelength at half-crest height

Besides the wave amplitude A, wavelength at half-crest height $\lambda_{1/2}$ is another wave characteristic of interest. The influence of higher-order free-surface nonlinearities on $\lambda_{1/2}$ under cases with different Fr_0, h_0/d and γ is investigated, respectively.

As shown in Fig. 18, the variation in wavelength at half-crest height $\lambda_{1/2}$ with respect to the Froude number based on the average water depth Fr_0 in both narrow and wide channels is nonmonotonic, and the width of the channel has little influence on the value of $\lambda_{1/2}/L$. As Fr_0 varies from 0.387 to 0.527, the value of $\lambda_{1/2}/L$ drops approximately from 3.20 to 2.55 in the HOS-VB models and falls from 3.12 to 2.08 in the linear model. However, as Fr_0 ranges from 0.527 to 0.562, $\lambda_{1/2}/L$ shows an increasing trend.

Comparing the values of $\lambda_{1/2}/L$ computed using the linear model and HOS-VB in each case, we observe that the higher-order free-surface nonlinearities cause an increase in wavelength.

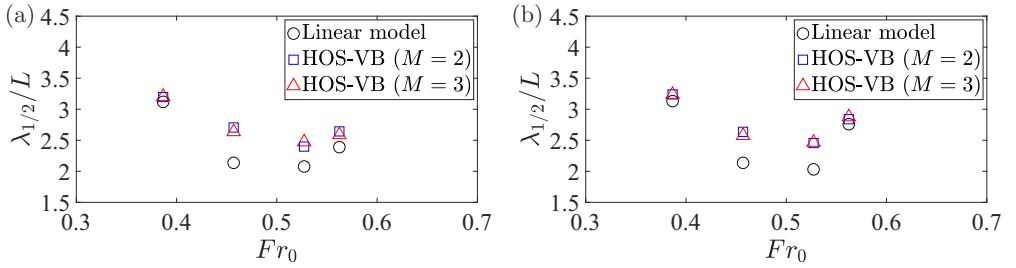

FIG. 18. Influence of free-surface nonlinearities on the wavelength at half-crest height $\lambda_{1/2}$ of mini-tsunamis in cases with different Froude numbers based on the average water depth: $\mathrm{Fr}_0 = 0.387$, 0.457, 0.527, and 0.562. (a) Results in the narrow channel with a width of $W/B = 4$. (b) Results in the wide channel with a width of $W/B = 20$.

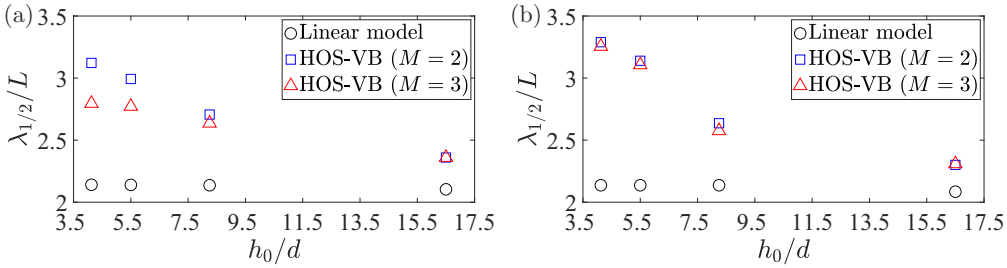

FIG. 19. Influence of free-surface nonlinearities on the wavelength at half-crest height $\lambda_{1/2}$ of mini-tsunamis in cases with different ratios of average water depth to the draft of ship: $h_0/d = 16.5$, 8.25, 5.5, and 4.125. (a) Results in the narrow channel with a width of $W/B = 4$. (b) Results in the wide channel with a width of $W/B = 20$.

Nonetheless, the values of $\lambda_{1/2}/L$ in HOS-VB with $M = 2$ and $M = 3$ are approximately the same for each case, which confirms that the major contribution comes from the second-order free-surface nonlinearities instead of the third-order nonlinearities. A relative depth kh can be estimated based on the wavelength at half-crest height $\lambda_{1/2}$ of mini-tsunamis and the water depth h_2 in shallow region, $kh = \pi h/\lambda_{1/2}$. In all the test cases, the maximum of kh is about 0.353, which means the relative depth is very small. The third-order nonlinearity is more significant in deep water instead of the shallow water, so third-order nonlinear effects are not significant in our test cases. Among the four cases with different Fr_0 values in the narrow or wide channel, the second-order free-surface nonlinear effects on $\lambda_{1/2}$ are the most significant when $\mathrm{Fr}_0 = 0.457$ and the increment is approximately 0.5 times the ship length.

Figure 19 illustrates the wavelength at half-crest height $\lambda_{1/2}$ under the different ratios of the average water depth to the draft of ship h_0/d. In both of the narrow and wide channels, the value of $\lambda_{1/2}/L$ obtained using the linear model is around 2.1, which hardly varies with h_0/d. However, the value of $\lambda_{1/2}/L$ obtained using HOS-VB ($M = 2, M_b = 5$) or HOS-VB ($M = 3, M_b = 5$) drops with h_0/d in both channels. The second-order free-surface nonlinearities play a leading role in the wavelength at half-crest height $\lambda_{1/2}$. Although the effects of the channel width on $\lambda_{1/2}/L$ is not prominent in the linear model, they are substantial in the HOS-VB when the ratio of average water depth to ship draft h_0/d is small, namely, for h_0/d in the range 4.125–5.5. The wavelength increase resulting from second- and third-order nonlinearities is more evident in the wide channel than that in the narrow channel. In particular, for deep draft case with $h_0/d = 4.125$ in the wide channel, the increase of $\lambda_{1/2}$ caused by the second- and third-order nonlinearities is a little bit more than the length of ship L.

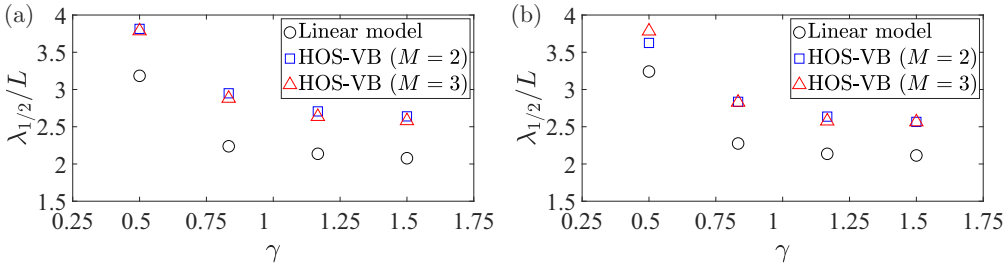

FIG. 20. Influence of free-surface nonlinearities on the wavelength at half-crest height $\lambda_{1/2}$ of mini-tsunamis with different slopes of the depth change: $\gamma = 0.5$, 0.833, 1.167, and 1.5. (a) Results in the narrow channel with a width of $W/B = 4$. (b) Results in the wide channel with a width of $W/B = 20$.

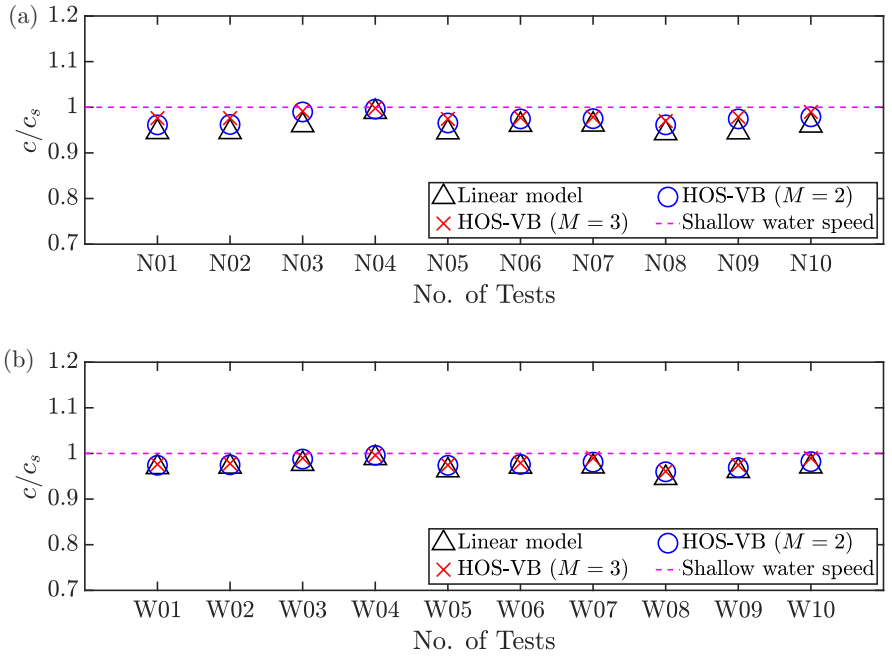

FIG. 21. Effect of free-surface nonlinearities on the phase velocity c of mini-tsunamis in all the test cases. The shallow water speed is $c_s = \sqrt{gh_2}$ where h_2 is the water depth of shallow region. (a) Narrow channel with a width of $W/B = 4$. (b) Wide channel with a width of $W/B = 20$.

The wavelength at half-crest height in the cases with different bottom variation slopes is shown in Fig. 20. As can be seen, the channel width has no evident influence on the wavelength at half-crest height. For both narrow and wide channels, $\lambda_{1/2}/L$ reduces as the slope of bottom variation γ rises from 0.5 to 0.833. However, when $\gamma > 0.833$, the decreasing trend of $\lambda_{1/2}/L$ with γ is suppressed. The increase in wavelength $\lambda_{1/2}$ induced by second- and third-order free-surface nonlinearities is approximately $0.55L$. In addition, because the increase of bottom variation slope γ induces an increase in wave amplitude and a decrease in wavelength at half-crest height, mini-tsunamis with larger steepness are formed as the depth change becomes steeper.

3. Effects of free-surface nonlinearities on phase velocity

As shown in Fig. 21, the phase velocity of the mini-tsunami in all the test cases ranges from $0.96\sqrt{gh_2}$ to $0.99\sqrt{gh_2}$, where h_2 is the shallow-water depth. Therefore, the factors of interest, that is, the width of channel, the Froude number based on the average water depth, the ratio of the average water depth to the draft of the ship, the slope of the bottom variation, and the free-surface nonlinearity, seem to have little influence on the phase velocity of the mini-tsunami. Instead, the phase velocity mainly depends on the shallow water depth.

VII. CONCLUSION

In this study, the nonlinear effects on mini-tsunamis, a new type of upstream wave generated when a ship moves from deep to shallow water at a subcritical speed, are investigated. The results obtained using the linear model proposed by Grue [1] and two nonlinear models, namely, HOS-VB and FUNWAVE-TVD, are compared. The influence of the width of the channel, Froude number Fr_0, ratio of the average water depth to the ship draft h_0/d, and slope of the bottom variation γ on the behavior of mini-tsunamis are systematically investigated.

First, the in-house HOS-VB codes are validated by the comparison of numerical results with the gauge records from an experiment and the data measured using a wave radar. HOS-VB ($M = 3$) shows a higher accuracy than the linear model in simulating upstream waves.

Then, the generation and propagation of mini-tsunamis are illustrated. After mini-tsunamis are generated, they propagate ahead of the ship at a speed comparable to the shallow-water speed. Several short waves follow the mini-tsunamis. The mean free-surface level of these short waves is significantly higher than the still-water level, which is mainly attributed to second-order nonlinearities.

Finally, the influence of bottom and free-surface nonlinearities in different test cases is analyzed. The wave amplitude is increased by both bottom and free-surface nonlinearities. Second-order free-surface nonlinearities play a major role and are more prominent in the narrow channel than that in the wide channel. Accordingly, they increase the wave amplitude by approximately 150% and 45% when $\mathrm{Fr}_0 = 0.562$ in the narrow and wide channels, respectively. The amplitude of mini-tsunamis increases with the Froude number Fr_0 according to Fr_0^{α} with α in the range of 4.2 to 6.3, and decreases with the ratio of average water depth to ship draft h_0/d according to $(h_0/d)^{\alpha}$ with α in the range of -1.4 to -1.2. The increasing trend of wave amplitude with Fr_0 and the decreasing trend of wave amplitude with h_0/d are more significant as the order of free-surface nonlinearities increases. The increasing rate of wave amplitude with bottom slope γ gradually tends to zero when $\gamma > 1.167$.

The wavelength is barely affected by the channel width and the bottom nonlinearities, while its increase owing to the free-surface nonlinearities is not more than the ship length. The nonlinear effects on the wavelength are enhanced as the ratio of average water depth to ship draft h_0/d decreases. We note that the wavelength at half-crest height decreases as the Froude number Fr_0 varies from 0.387 to 0.527, but increases as Fr_0 changes from 0.527 to 0.562. Moreover, the wavelength at half-crest height declines with the ratio of average water depth to ship draft h_0/d. As bottom slope γ increases within a range of less than 0.833, the wave amplitude increases but the wavelength decreases, so a larger bottom slope can induce mini-tsunamis with a greater steepness. However, both wave amplitude and wavelength remain almost constant when $\gamma > 0.833$.

ACKNOWLEDGMENTS

The present work is sponsored by the Oceanic Interdisciplinary Program of Shanghai Jiao Tong University (Project No. SL2021PT205). X.Z. and J.Y. gratefully acknowledge the financial support from the National Natural Science Foundation of China under Grant No. 52171269. X.Z. appreciates valuable discussions with Prof. Zhongbo Liu at Dalian Maritime University.

APPENDIX A: LOW-PASS FILTER OF HOS-VB

A low-pass filter is used to control the sawtooth instabilities caused by aliasing in the high-order spectral method. In HOS-VB, a filter which is similar to that employed by Xiao [31] is adopted. For convenience, we refer this as the Filter-VB. This filter is applied to η and ϕ in the Fourier space and is in the form of a exponential function,

$$\Lambda(k_x, k_y | k_{xc}, k_{yc}) = \exp\left\{\left[\left(\frac{k_x}{k_{xc}}\right)^2 + \left(\frac{k_y}{k_{yc}}\right)^2\right]^{\frac{n}{2}}\right\}, \tag{A1}$$

where the parameter n equals to 30. The wave number vector of each component is $\mathbf{k} = (k_x, k_y)$. k_{xc} and k_{yc} are the cutoff wave numbers in the x and y directions, respectively. Their definitions, namely, $k_{xc} = \tau_1 k_w$ and $k_{yc} = \tau_2 k_w$, are related to the wave number of the mini-tsunamis k_w, which can be estimated in the first attempt of numerical calculation. The definition of the wave number of the mini-tsunami is $k_w = \pi / \lambda_{1/2}$, where $\lambda_{1/2}$ is the wavelength at half-crest height of the mini-tsunami. Therefore, τ_1 and τ_2 are the two unknowns in Filter-VB that need to be determined. As τ_1 and τ_2 are critical to ensure the reliability of the numerical results, a sensitivity study is performed.

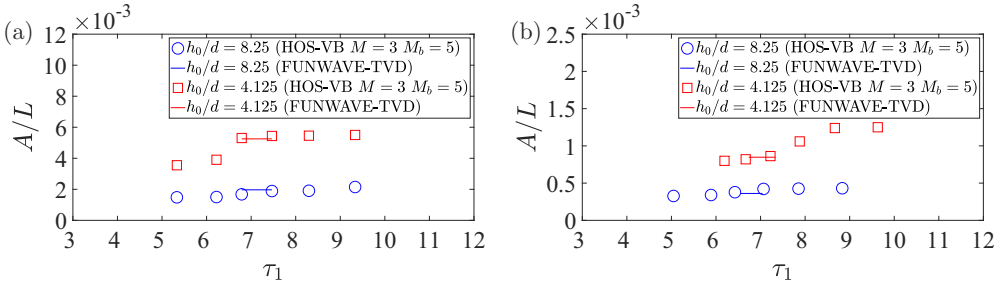

FIG. 22. Sensitivity test of τ_1. Symbols are the results computed by HOS-VB ($M = 3$, $M_b = 5$) with different values of τ_1. $\tau_2 = 5$ is used. The solid line represents the results obtained using FUNWAVE-TVD. The blue and the red markers in panel (a) represent the two cases with $\mathrm{Fr}_0 = 0.457$ in a narrow channel, Tests N02 and N07, respectively. The blue and the red markers in panel (b) are for the two cases with $\mathrm{Fr}_0 = 0.457$ in a wide channel, Tests W02 and W07, respectively.

We choose four cases with different ratios of the average water depth to ship draft h_0/d (namely, Tests N02, N07, W02, and W07 in Table I) for the sensitivity test, and the results are shown in Figs. 22 and 23. The first two cases are studied for the narrow channel, while the other two are studied for the wide channel. In each case, the results obtained using HOS-VB ($M = 3$, $M_b = 5$) with different parameter values in Filter-VB are compared with those obtained using FUNWAVE-TVD, which are used as reference. We determine that $\tau_1 = 7$ and $\tau_2 = 5$ are the most suitable values. With these values of the parameters in Filter-VB, the results computed using HOS-VB ($M = 3$, $M_b = 5$) in different test cases show satisfactory agreement with those using FUNWAVE-TVD.

In addition, note that the cutoff wave numbers in the x and y directions, that is, $k_{xc} = 7k_w$ and $k_{yc} = 5k_w$, should follow the $half - rule$ which is used to address the aliasing error [32]. Additionally, the maximum wave number $k_{\max} = \sqrt{(\pi N_x/L_x)^2 + (\pi N_y/L_y)^2}$ must be at least twice the value of the cutoff wave number $k_c = \sqrt{k_{xc}^2 + k_{yc}^2}$.

APPENDIX B: ANALYSIS OF THE ORDER OF BOTTOM NONLINEARITY IN HOS-VB ($M = 1$)

Here we compare the linear model proposed by Grue [1] with the HOS-VB ($M = 1$), where $M = 1$ indicates that the linear free-surface boundary condition is adopted.

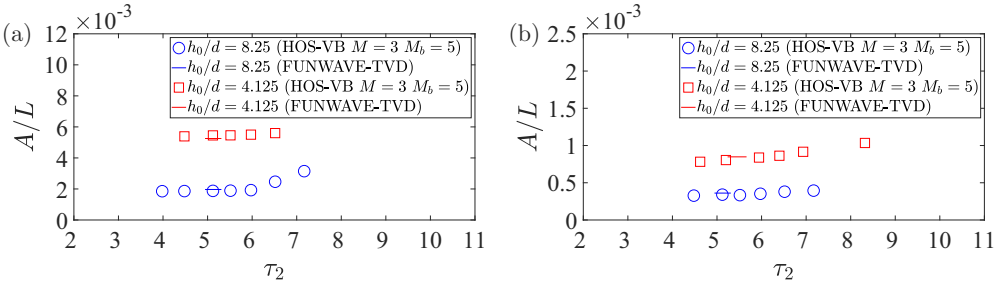

FIG. 23. Sensitivity test of τ_2. Symbols are the results computed by HOS-VB ($M = 3$, $M_b = 5$) with different values of τ_2. $\tau_1 = 7$ is used. The solid line represents the results obtained using FUNWAVE-TVD. The blue and the red markers in panel (a) correspond to the two cases with $\mathrm{Fr}_0 = 0.457$ in a narrow channel, Tests N02 and N07, respectively. The blue and the red markers in panel (b) are for the two cases with $\mathrm{Fr}_0 = 0.457$ in a wide channel, Tests W02 and W07, respectively.

Because the normal velocity of water on the bottom is closely related to the generation of mini-tsunamis, we compare the mathematical expression of the normal velocity at the bottom V_b in the linear model and HOS-VB ($M = 1$) with different orders of bottom nonlinearity M_b. According to Eq. (3) in Grue *et al.* [23], the normal velocity on the bottom in the linear model is expressed by

$$V_b^{\mathrm{G}} = \nabla \cdot [\beta \nabla (\phi_{0,B} + \phi_{\beta,B})], \tag{B1}$$

where $\nabla = (\frac{\partial}{\partial x}, \frac{\partial}{\partial y})$, β is the depth variation, and $\phi_{0,B}$ and $\phi_{\beta,B}$ are the bottom potentials according to the average depth and the bottom potentials caused by the depth variations, respectively. In HOS-VB, the bottom boundary condition described in Eq. (4) is expanded around the average water depth, $z = -h_0$. With Eqs. (6) and (7), the normal velocity on the bottom is written as

$$V_b^{\mathrm{H}} = \frac{\partial \phi^{(1)}}{\partial z} = \frac{\partial \phi_{h_0}^{(1)}}{\partial z} + \frac{\partial \phi_{\beta}^{(1)}}{\partial z} = \frac{\partial \phi_{\beta}^{(1)}}{\partial z} = \sum_{l=1}^{M_b} \left(\frac{\partial \phi_{\beta}^{(1,l)}}{\partial z} \right), \quad \text{on } z = -h_0, \tag{B2}$$

where ϕ_{h_0} and ϕ_{β} are the potentials defined in Eq. (6). The expression of Eq. (B2) for the each order of l can be derived from Eq. (12). If Eq. (B2) is truncated to $M_b = 1$, the normal velocity on the bottom in HOS-VB ($M = 1, M_b = 1$) is

$$V_b^{\mathrm{H1}} = \frac{\partial \phi_{\beta}^{(1,1)}}{\partial z} = \nabla \beta \cdot \nabla \phi_{h_0}^{(1)} + \beta \nabla^2 \phi_{h_0}^{(1)} = \nabla \cdot \left(\beta \nabla \phi_{h_0}^{(1)} \right). \tag{B3}$$

If Eq. (B2) is truncated to $M_b = 2$, the normal velocity on the bottom in HOS-VB ($M = 1$, $M_b = 2$) is

$$V_b^{\mathrm{H2}} = \frac{\partial \phi_{\beta}^{(1,1)}}{\partial z} + \frac{\partial \phi_{\beta}^{(1,2)}}{\partial z} = \nabla \cdot \left[\beta \nabla \left(\phi_{h_0}^{(1)} + \phi_{\beta}^{(1,1)} \right) \right]. \tag{B4}$$

Note that the physical meanings of $\phi_{h_0}^{(1)}$ and $\phi_{\beta}^{(1,1)}$ in HOS-VB are similar to those of $\phi_{0,B}$ and $\phi_{\beta,B}$ in the linear model, respectively. Compared to V_b^{G}, V_b^{H1} lacks the term about the potential induced by the depth change, $\phi_{\beta}^{(1,1)}$, while V_b^{H2} includes the contribution from both $\phi_{h_0}^{(1)}$ and $\phi_{\beta}^{(1,1)}$. Therefore, the results computed using HOS-VB ($M = 1, M_b = 2$), instead of HOS-VB ($M = 1, M_b = 1$), are equivalent to those obtained using the linear model.

[1] J. Grue, Ship generated mini-tsunamis, J. Fluid Mech. **816**, 142 (2017).

[2] K. E. Parnell and H. Kofoed-Hansen, Wakes from large high-speed ferries in confined coastal waters: Management approaches with examples from New Zealand and Denmark, Coast. Manage **29**, 217 (2001).

[3] K. E. Parnell, T. Soomere, L. Zaggia, A. Rodin, G. Lorenzetti, J. Rapaglia, and G. M. Scarpa, Ship-induced solitary Riemann waves of depression in Venice Lagoon, Phys. Lett. A **379**, 555 (2015).

[4] T. Constantine, On the movement of ships in restricted waterways, J. Fluid Mech. **9**, 247 (1960).

[5] E. O. Tuck, Shallow-water flows past slender bodies, J. Fluid Mech. **26**, 81 (1966).

[6] J. V. Wehausen, The wave resistance of ships, Adv. Appl. Mech. **13**, 93 (1973).

[7] R. F. Beck, J. N. Newman, and E. O. Tuck, Hydrodynamic forces on ships in dredged channels, J. Ship Res. **19**, 166 (1975).

[8] T. Y. Wu and D. M. Wu, Three-dimensional nonlinear long waves due to moving surface pressure, in *Proceedings of the 14th Symposium on Naval Hydrodynamics* (National Academy of Sciences, Washington DC, 1982), pp. 103–125.

[9] T. Y. Wu, Generation of upstream advancing solitons by moving disturbances, J. Fluid Mech. **184**, 75 (1987).

[10] S. L. Cole, Transient waves produced by flow past a bump, Wave Motion **7**, 579 (1985).

[11] X. Chen and S. D. Sharma, A slender ship moving at a near-critical speed in a shallow channel, J. Fluid Mech. **291**, 263 (1995).

[12] R. C. Ertekin, W. C. Webster, and J. V. Wehausen, Ship-generated solitons, in *Proceedings of the 15th Symposium of Naval Hydrodynamics* (National Academy of Sciences, Hamburg, 1984), pp. 22–36.
[13] Y. Li and P. D. Sclavounos, Three-dimensional nonlinear solitary waves in shallow water generated by an advancing disturbance, J. Fluid Mech. **470**, 383 (2002).
[14] C. Ai, Y. Ma, L. Sun, and G. Dong, Numerical simulation of ship waves in the presence of a uniform current, Coastal Eng. **179**, 104250 (2023).
[15] R. Grimshaw, The solitary wave in water of variable depth, J. Fluid Mech. **42**, 639 (1970).
[16] P. A. Madsen and O. R. Sørensen, A new form of the Boussinesq equations with improved linear dispersion characteristics. Part 2. A slowly-varying bathymetry, Coastal Eng. **18**, 183 (1992).
[17] S. Agarwal, V. Sriram, P.-F. Liu, and K. Murali, Waves in waterways generated by moving pressure field in Boussinesq equations using unstructured finite element model, Ocean Eng. **262**, 112202 (2022).
[18] G. Wei, J. T. Kirby, S. T. Grilli, and R. Subramanya, A fully nonlinear Boussinesq model for surface waves. Part 1. Highly nonlinear unsteady waves, J. Fluid Mech. **294**, 71 (1995).
[19] T. Torsvik, G. Pedersen, and K. Dysthe, Influence of cross channel depth variation on ship wave patterns, J. Mech. Appl. Math. **2**, 1 (2008).
[20] M. F. Nascimento, C. F. Neves, and G. F. Maciel, Propagation of ship waves on a sloping bottom, in *Proceedings of the 31st International Conference on Coastal Engineering* (World Scientific, Hamburg, 2009), pp. 696–708.
[21] K. A. Belibassakis, A coupled-mode technique for the transformation of ship-generated waves over variable bathymetry regions, Appl. Ocean Res. **25**, 321 (2003).
[22] C. G. David, V. Roeber, N. Goseberg, and T. Schlurmann, Generation and propagation of ship-borne waves—Solutions from a Boussinesq-type model, Coastal Eng. **127**, 170 (2017).
[23] J. Grue, G. K. Pedersen, and Ø. Saetra, Free wave effects in meteotsunamis, JGR Oceans **127**, e2021JC017669 (2022).
[24] J. Zhang, M. Benoit, O. Kimmoun, A. Chabchoub, and H.-C. Hsu, Statistics of extreme waves in coastal waters: Large scale experiments and advanced numerical simulations, Fluids **4**, 99 (2019).
[25] J. Zhang and M. Benoit, Wave-bottom interaction and extreme wave statistics due to shoaling and de-shoaling of irregular long-crested wave trains over steep seabed changes, J. Fluid Mech. **912**, A28 (2020).
[26] B. West, K. Brueckner, R. S. Janda, D. M. Milder, and R. L. Milton, A new numerical method for the surface hydrodynamics, J. Geophys. Res. **92**, 11803 (1987).
[27] D. G. Dommermuth and D. K. P. Yue, A high-order spectral method for the study of nonlinear gravity waves, J. Fluid Mech. **184**, 267 (1987).
[28] M. Gouin, G. Ducrozet, and P. Ferrant, Propagation of 3D nonlinear waves over an elliptical mound with a high-order spectral method, Eur. J. Mech. B Fluids **63**, 9 (2017).
[29] F. Shi, J. T. Kirby, J. C. Harris, J. D. Geiman, and S. T. Grilli, A high-order adaptive time-stepping TVD solver for Boussinesq modeling of breaking waves and coastal inundation, Ocean Model. **43–44**, 36 (2012).
[30] F. Shi, M. Malej, J. M. Smith, and J. T. Kirby, Breaking of ship bores in a Boussinesq-type ship-wake model, Coastal Eng. **132**, 1 (2018).
[31] W. Xiao, Study of directional ocean wavefield evolution and rogue wave occurrence using large-scale phase-resolved nonlinear simulations, Ph.D. thesis, Massachusetts Institute of Technology, Cambridge, MA, 2013.
[32] F. Bonnefoy, G. Ducrozet, D. L. Touzé, and P. Ferrant, Time-domain simulation of nonlinear water waves using spectral methods, in *Advances in Numerical Simulation of Nonlinear Water Waves* (World Scientific, London, 2010), pp. 129–164.